GEOPHYSICS, VOL. 72, NO. 6 (NOVEMBER-DECEMBER 2007); P. A87–A91, 6 FIGS.
10.1190/1.2781582

Stereographic imaging condition for wave-equation migration

Paul Sava[1]

ABSTRACT

Imaging under the single-scattering approximation consists of two steps: wavefield reconstruction of source and receiver wavefields from simulated and recorded data, respectively, and imaging from the extrapolated wavefields of locations where reflectors occur. Conventionally, the imaging condition indicates the presence of reflectors when propagation times of reflections in the source and receiver wavefields match. The main drawback of a conventional crosscorrelation imaging condition is that it ignores the local spatial coherence of reflection events and relies only on their propagation time. This leads to interference between unrelated events that occur at the same time. Sources of crosstalk include seismic events corresponding to different seismic experiments, propagation paths, types of reflections (primary or multiple), or wave modes (P or S). An alternative imaging condition operates on the same extrapolated wavefields, but crosscorrelation takes place in a higher-dimension domain where seismic events are separated based on their local space-time slope. Events are matched based on two parameters (time and local slope), thus justifying the name "stereographic" for this imaging condition. Stereographic imaging attenuates wavefield crosstalk and reduces imaging artifacts compared with conventional imaging. Applications of the stereographic imaging condition include simultaneous imaging of multiple seismic experiments, multiple attenuation in the imaging condition, and attenuation of crosstalk between multiple wavefield branches or multiple wave modes.

INTRODUCTION

Conventional depth migration consists of two steps: seismic wavefield reconstruction at all locations in the imaging volume from surface data and imaging used to extract reflectivity information from wavefields reconstructed from sources and receivers. Accurate imaging requires accurate implementation of both steps. Recent seismic imaging research places greater emphasis on wavefield extrapolation than on imaging, partly because of the higher computational cost of extrapolation relative to imaging.

This paper concentrates on the imaging condition, assuming that wavefield extrapolation is performed in a sufficiently accurate velocity model. The imaging condition is often implemented as a crosscorrelation of source and receiver wavefields extrapolated from the acquisition surface (Claerbout, 1985). The reason for this choice is that conventional crosscorrelation imaging is fast and robust, producing good images in complex environments. The alternative deconvolution imaging condition is not discussed here.

The conventional imaging condition operates in a simple way: Source and receiver wavefields are probed to determine the locations where they match, i.e., where the traveltime of events forward-propagated from the source and backward-propagated from the receivers are equal. This is usually achieved by extracting the zero lag of the temporal crosscorrelation between the two wavefields computed at every location in the image. However, this imaging condition ignores the structure of the analyzed seismic wavefields, i.e., the imaging condition does not use the local space-time coherence of the reflected wavefields. This characteristic is contrary to conventional analysis of space-time kinematic coherence of seismic data, which is one of the most important attributes used in their analysis.

The consequence of this deficiency is that different seismic events present in the extrapolated wavefields interfere with one another leading to artifacts in seismic images. This interference, also known as crosstalk, occurs between unrelated events that should not contribute to the formed image. It is often possible to identify events that occur at the same time, even though they describe different propagation paths in the subsurface. As a consequence, such unrelated events appear as real reflections because of the imaging condition rather than a geologic cause.

This paper extends of the conventional imaging condition, designed to exploit the local space-time coherence of extrapolated wavefields. Different seismic events are matched as a function of propagation time and by local coherence attributes, e.g., local slope measured as a function of position and time. Therefore, events with different propagation paths are differentiated from one another, although their propagating time to a given point in the subsurface may

Manuscript received by the Editor 2 May 2007; revised manuscript received 7 June 2007; published online 18 September 2007.
[1]Colorado School of Mines, Department of Geophysics, Golden, Colorado. E-mail: psava@mines.edu.

be identical. This property can be used to suppress artifacts arising from crosstalk, generating cleaner seismic images.

CONVENTIONAL IMAGING CONDITION

Under the single-scattering (Born) approximation, seismic migration consists of two components: wavefield reconstruction and imaging.

Wavefield reconstruction forms solutions to the considered (acoustic) wave equation with recorded data as boundary condition. One can consider many different numeric solutions to the acoustic wave equation, which are distinguished, for example, by implementation domain (e.g., space-time, frequency-wavenumber) or type of numeric solution (e.g., differential, integral). Irrespective of numeric implementation, two wavefields are reconstructed, one forward-propagated from the source and one backward-propagated from the receiver locations. These wavefields can be represented as 4D objects as a function of position in space $\mathbf{x} = (x,y,z)$ and time t:

$$U_S = U_S(\mathbf{x},t), \tag{1}$$

$$U_R = U_R(\mathbf{x},t), \tag{2}$$

where U_S and U_R denote source and receiver wavefields. For the remainder of this paper, I assume that the two wavefields have been reconstructed with one of the numerical methods mentioned earlier.

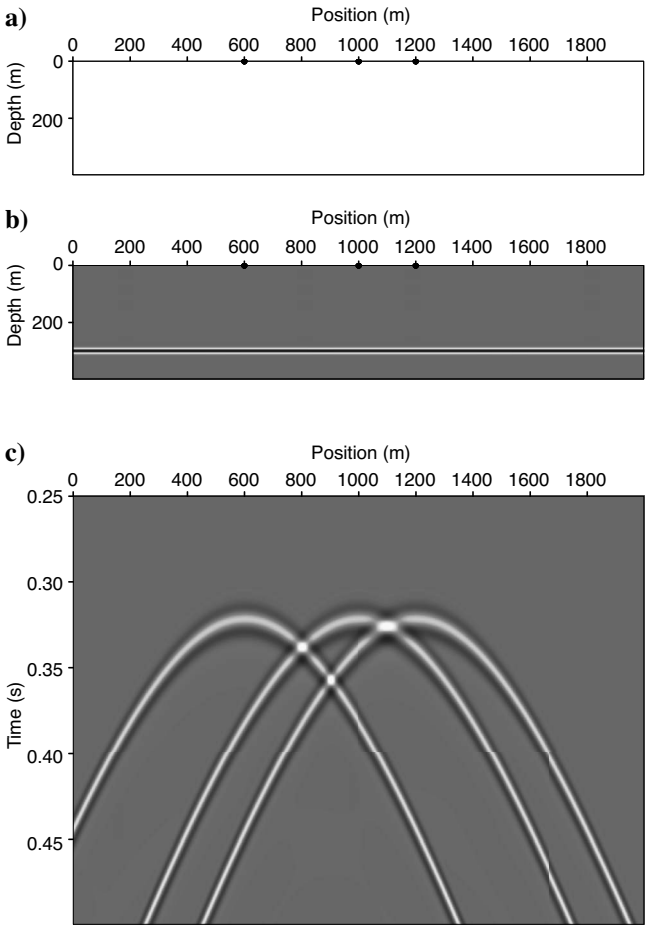

Figure 1. (a) Constant-velocity model, (b) reflectivity model, and (c) data and shot locations at $x = 600, 1000, 1200$ m.

The second migration component is the imaging condition designed to extract the locations of subsurface reflectors from the extrapolated wavefields (U_S and U_R). Image R can be extracted from the extrapolated wavefields by evaluating the match between the source and receiver wavefields at every location in the subsurface. The wavefield match can be evaluated using an extended imaging condition (Sava and Fomel, 2005, 2006), where R represents an estimate of the similarity between the source and receiver wavefields in all four dimensions, space ($\mathbf{x}$) and time (t):

$$R(\mathbf{x},\boldsymbol{\lambda},\tau) = \int U_S(\mathbf{x}-\boldsymbol{\lambda},t-\tau)U_R(\mathbf{x}+\boldsymbol{\lambda},t+\tau)dt. \tag{3}$$

The quantities $\boldsymbol{\lambda}$ and τ represent the spatial and temporal crosscorrelation lags between the source and receiver wavefields. The source and receiver wavefields are coincident (i.e., form an image) if the local crosscorrelation between the source and receiver wavefields maximizes at zero lag in all four dimensions.

Other extended imaging conditions (Rickett and Sava, 2002; Biondi and Symes, 2004) represent special cases of the extended imaging condition corresponding to horizontal $\boldsymbol{\lambda} = (\boldsymbol{\lambda}_x,\boldsymbol{\lambda}_y,0)$, or vertical $\boldsymbol{\lambda} = (0,0,\boldsymbol{\lambda}_z)$ space lags, respectively. The conventional imaging condition (Claerbout, 1985) is also a special case of the extended imaging condition 3, corresponding to zero crosscorrelation lag in space ($\boldsymbol{\lambda} = 0$) and time ($\boldsymbol{\tau} = 0$):

$$R(\mathbf{x}) = \int U_S(\mathbf{x},t)U_R(\mathbf{x},t)dt. \tag{4}$$

The 4D crosscorrelation 3 maximizes at zero lag if the source and receiver wavefields are reconstructed correctly. If this is not true, either because one is using an approximate extrapolation operator (e.g., one-way extrapolator with limited angular accuracy) or because the velocity used for extrapolation is inaccurate, then the 4D crosscorrelation does not maximize at zero lag and part of the crosscorrelation energy is smeared over space and time lags ($\boldsymbol{\lambda}$ and τ). Therefore, extended imaging conditions can be used to evaluate imaging accuracy — for example, by decomposing the reflectivity as a function of scattering angle at every image location (Sava and Fomel, 2003; Biondi and Symes, 2004; Sava and Fomel, 2006). Angle-domain images carry information useful for migration velocity analysis (Biondi and Sava, 1999; Sava and Biondi, 2004a,b; Shen et al., 2005), amplitude analysis (Sava et al., 2001), or attenuation of multiples (Sava and Guitton, 2005; Artman et al., 2007).

This paper focuses on the conventional imaging condition 4. As discussed, assuming accurate extrapolation, this imaging condition should produce accurate images at zero crosscorrelation lags. However, this conclusion does not always hold true, as illustrated next.

Figure 1a and b represents a simple model of constant velocity with a horizontal reflector. Data in this model are simulated from three sources triggered simultaneously at coordinates $x = 600$, 1000, 1200 m (Figure 1c). Using the standard imaging procedure outlined above, one can reconstruct the source and receiver wavefields U_S and U_R, and apply the conventional imaging condition equation 4 to obtain the image in Figure 2a. The image shows the horizontal reflector superimposed with linear artifacts of comparable strength.

Figure 3a and b represents another simple model of spatially variable velocity with a horizontal reflector. Data in this model are simulated from a source located at coordinate $x = 1000$ m (Figure 3c). The negative Gaussian velocity anomaly present in the velocity

model creates triplications of the source and receiver wavefields. Using the same standard imaging procedure, one obtains the image in Figure 4a, also illustrating the horizontal reflector superimposed with complex artifacts of comparable strength.

In both cases, the velocity model is known perfectly and the acoustic wave equation is solved with the same finite-difference operator implemented in the space-time domain. Therefore, artifacts are caused only by properties of the conventional imaging condition used to produce the migrated image and not by inaccuracies of wavefield extrapolation or of the velocity model.

Artifacts are caused by crosstalk between events present in the source and receiver wavefields, which are not supposed to match. For example, crosstalk can occur between wavefields corresponding to multiple sources (Figures 1a and b), multiple branches of a wavefield corresponding to one source (Figures 3a and b), events that correspond to multiple reflections in the subsurface, or multiple wave modes of an elastic wavefield — for example, between PP and PS reflections.

STEREOGRAPHIC IMAGING CONDITION

One possibility to remove artifacts caused by crosstalk between inconsistent reflection events is to modify the imaging condition to use more than one attribute for matching the source and receiver wavefields. For example, one could use time and slope to match events in the wavefield, thus distinguishing between unrelated events that occur at the same time (Figure 5).

A simple way of decomposing the source and receiver wavefields as a function of local slope at every position and time is by local slant stacks at coordinates $\mathbf{x}$ and t in the 4D source and receiver wavefields. Thus, one can write the total source and receiver wavefields (U_S and U_R) as a sum of decomposed wavefields (W_S and W_R):

$$U_S(\mathbf{x},t) = \int W_S(\mathbf{x},\mathbf{p},t)d\mathbf{p}, \tag{5}$$

$$U_R(\mathbf{x},t) = \int W_R(\mathbf{x},\mathbf{p},t)d\mathbf{p}. \tag{6}$$

Here, the 3D vector $\mathbf{p}$ represents the local slope function of position and time. Using the wavefields decomposed as a function of local slope, W_S and W_R, one can design a stereographic imaging condition that crosscorrelates the wavefields in the decomposed domain, followed by summation over the decomposition variable:

$$R(\mathbf{x}) = \int\int W_S(\mathbf{x},\mathbf{p},t)W_R(\mathbf{x},\mathbf{p},t)d\mathbf{p}dt. \tag{7}$$

Correspondence between the slopes $\mathbf{p}$ of the decomposed source-receiver wavefields occurs only in planes dipping with the slope of

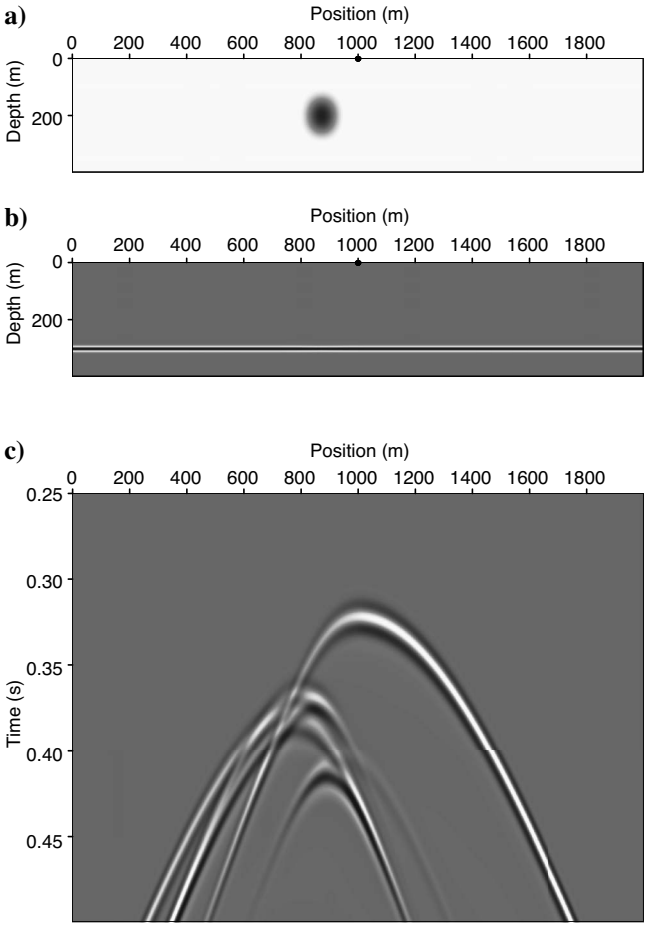

Figure 3. (a) Velocity model with a negative Gaussian anomaly, (b) reflectivity model, and (c) data and shot location at $x = 1000$ m.

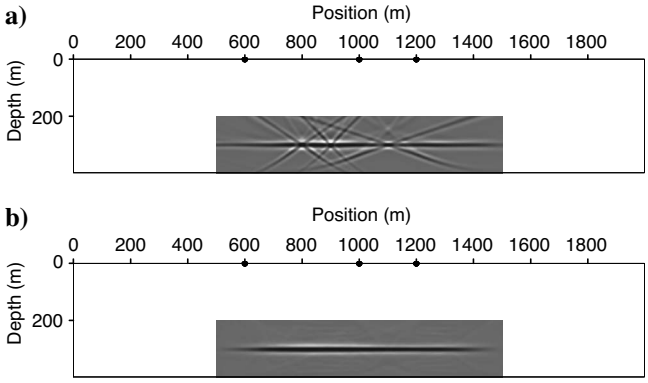

Figure 2. Images obtained for the model in Figure 1 using (a) the conventional imaging condition and (b) the stereographic imaging condition.

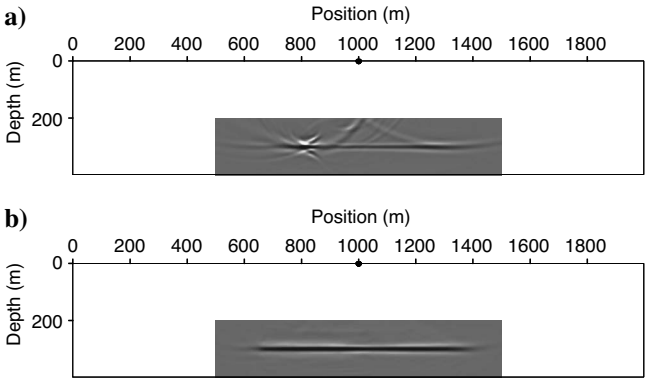

Figure 4. Images obtained for the model in Figure 3 using (a) the conventional imaging condition and (b) the stereographic imaging condition.

the imaged reflector at every location in space. Therefore, an approximate measure of the expected reflector slope is required for correct comparison of corresponding reflection data in the decomposed wavefields.

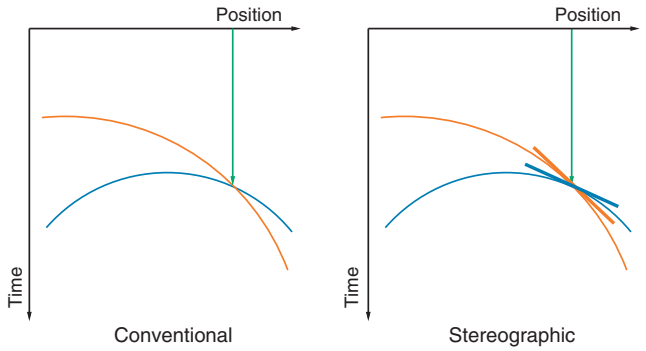

Figure 5. Comparison of (a) conventional imaging and (b) stereographic imaging.

The choice of the word "stereographic" for this imaging condition is analogous to that made for the velocity estimation method called stereotomography (Billette and Lambaré, 1997; Billette et al., 2003), which uses two parameters (time and slope) to constrain traveltime seismic tomography.

For comparison with the stereographic imaging condition 7, the conventional imaging condition can be reformulated using wavefield notation 5 and 6 as follows:

$$R(\mathbf{x}) = \int \left[\int W_S(\mathbf{x},\mathbf{p},t)d\mathbf{p} \right] \left[\int W_R(\mathbf{x},\mathbf{p},t)d\mathbf{p} \right] dt. \quad (8)$$

The main difference between imaging conditions 7 and 8 is that one case compares independent slope components of the wavefields separated from one another, and the other case compares a superposition of them, not distinguishing between waves propagating in different directions. This is analogous to the reflectivity analysis function of scattering angle at image locations, in contrast with the reflectivity analysis function of acquisition offset at the surface. In the first case, waves propagating in different directions are separated from one another; in the second case, all waves are superimposed in the data, leading to imaging artifacts (Stolk and Symes, 2004).

Figure 2b shows the image produced by stereographic imaging of the data generated for the model depicted in Figure 1a and b, and Figure 4b shows a similar image for the model depicted in Figure 3a and b. Images 2b and 4b use the same source-receiver wavefields as images 2a and 4a, respectively. In both cases, crosstalk artifacts have been eliminated by the stereographic imaging condition.

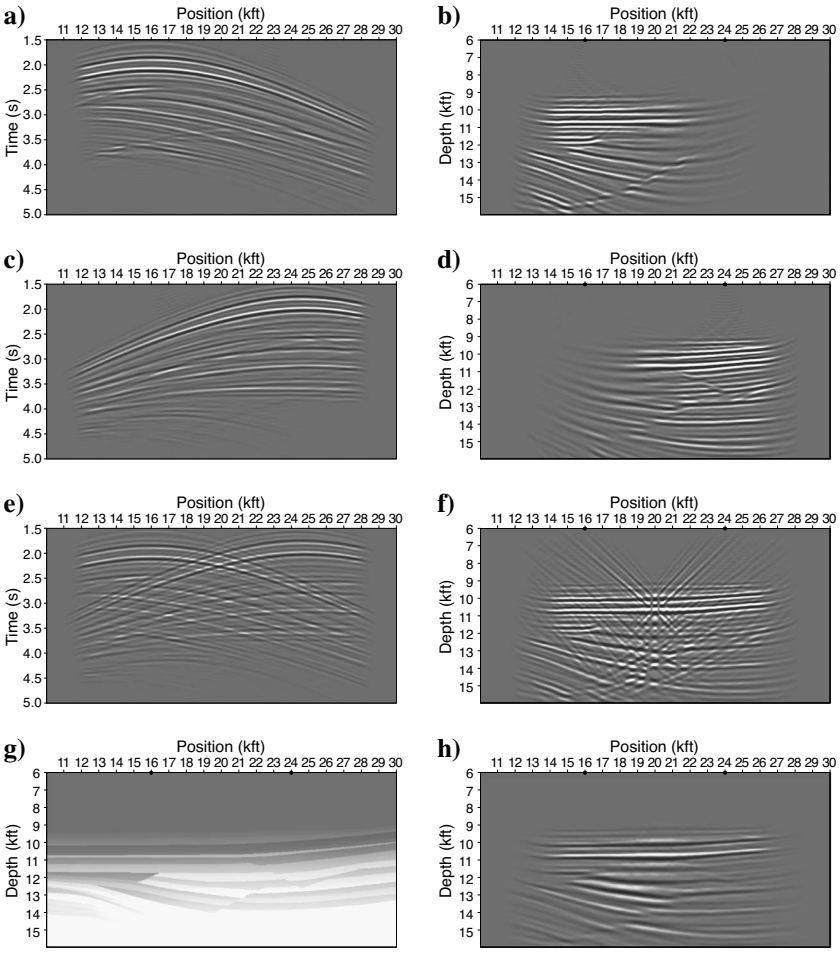

Figure 6. (a) Data corresponding to a shot located at $x = 16$ kft (4.83 km). (b) Image obtained by conventional imaging condition for (a). (c) Data corresponding to a shot located at $x = 24$ kft (7.25 km). (d) Image obtained by conventional imaging condition for (c). (e) Sum of data corresponding to shots in (a) and (c). (f) Image obtained by conventional imaging condition for data in panel (e). (g) Velocity model extracted from the Sigsbee 2A model. (h) Image obtained by the stereographic imaging condition for data in (e).

EXAMPLE

The stereographic imaging condition is illustrated with an example derived from the Sigsbee 2A data set (Paffenholz et al., 2002). Using the model in Figure 6g, two shots are simulated by wavefield extrapolation modeling (Figure 6a and c), and a third shot is synthesized by summing the two shots together (Figure 6e). Migration with a conventional imaging condition of the three shots produces the images in Figure 6b, d, and f for data in Figure 6a, c, and e, respectively. The two shots independently illuminate different parts of the model (Figure 6b and d), and the third composite shot illuminates both sides of the image (Figure 6f). The image produced by the composite shot is populated with artifacts from crosstalk between the wavefields originating at the two shot locations.

Figure 6h shows the image obtained by imaging the composite shot (Figure 6e), using the stereographic imaging condition. The image is free of artifacts and shows reflectors extending over the entire image, as would be expected for illumination from two shots at different locations. In this case, the stereographic imaging condition needs to account for the local dip of the image.

Because the reflector dip prior to application of the imaging condition is not known exactly, one must to loop over a range of possible dip angles in the vicinity of the expected reflector dip. Thus, the stereographic imaging procedure matches the dip of wavefield components in local windows around every image point. Assuming the local geologic dip is known, one can use this exact information to avoid looping over angle and decrease the cost of the imaging condition. This approach remains to be investigated by future research.

DISCUSSION

The imaging procedure described in this paper requires additional steps that add to the computing cost of imaging. Furthermore, there are more parameters that must be chosen. For example, if one uses local slant stacks for local decomposition, one must decide how many local slopes to use, how finely to sample the slope parameters, and how finely in space to apply slant stacking of the source-receiver wavefields. The number of local slopes used for the imaging condition depends on wavefield sampling in space and time in order to avoid aliasing. Those challenges remain to be addressed by future.

In all examples described in this paper, the local windows have a simple rectangular shape. However, more sophisticated window types (e.g., Gaussian) are possible alternatives and might improve the method's quality and efficiency.

One can consider tuning the stereographic imaging condition for specific applications. In current implementation, only image components with spatial coherence (e.g., reflectors) generate wavefields with spatial coherence. Diffractions, for example, do not fit this description and thus are removed from the image by the imaging condition. This can be seen as a feature or as a drawback, depending on the type of imaging target.

CONCLUSIONS

Conventional imaging conditions based on crosscorrelation of extrapolated wavefields do not take into account the local spatial coherence of reflection events. Events are matched based on their propagation times, which leads to crosstalk between unrelated events. The stereographic imaging condition introduced here operates on seismic wavefields that are first decomposed as a function of their local slope in space and time. Events are matched based on two parameters (time and local slope), which separates unrelated events and eliminates crosstalk. Higher imaging accuracy is achieved at the expense of greater computational cost. Applications include simultaneous imaging of different seismic experiments (shots) and multiple attenuation in the imaging condition.

ACKNOWLEDGMENT

This work is supported by the sponsors of the Center for Wave Phenomena at Colorado School of Mines.

REFERENCES

Artman, B., G. Alvarez, and K. Matson, 2007, Image-space surface-related multiple prediction: Geophysics, **72**, no. 2, S113–S122.

Billette, F., S. L. Begat, P. Podvin, and G. Lambaré, 2003, Practical aspects and applications of 2D stereotomography: Geophysics, **68**, 1008–1021.

Billette, F., and G. Lambaré, 1997, Velocity macro model estimation by stereotomography: 59th Annual Conference and Technical Exhibition, EAGE, Extended Abstracts, Session: P095.P095.

Biondi, B., and P. Sava, 1999, Wave-equation migration velocity analysis: 69th Annual International Meeting, SEG, Expanded Abstracts, 1723–1726.

Biondi, B., and W. W. Symes, 2004, Angle-domain common-image gathers for migration velocity analysis by wavefield-continuation imaging: Geophysics, **69**, 1283–1298.

Claerbout, J. F., 1985, Imaging the earth's interior: Blackwell Scientific Publications, Inc.

Paffenholz, J., B. McLain, J. Zaske, and P. Keliher, 2002, Subsalt multiple attenuation and imaging: Observations from the Sigsbee2B synthetic data set: 72nd Annual International Meeting, SEG, Expanded Abstracts, 2122–2125.

Rickett, J., and P. Sava, 2002, Offset and angle-domain common image-point gathers for shot-profile migration: Geophysics, **67**, 883–889.

Sava, P., and B. Biondi, 2004a, Wave-equation migration velocity analysis I: Theory: Geophysical Prospecting, **52**, 593–606.

——–, 2004b, Wave-equation migration velocity analysis II: Subsalt imaging examples: Geophysical Prospecting, **52**, 607–623.

Sava, P., B. Biondi, and S. Fomel, 2001, Amplitude-preserved common image gathers by wave-equation migration: 71st Annual International Meeting, SEG, Expanded Abstracts, 296–299.

Sava, P., and S. Fomel, 2003, Angle-domain common image gathers by wavefield continuation methods: Geophysics, **68**, 1065–1074.

——–, 2005, Coordinate-independent angle-gathers for wave equation migration: 75th Annual International Meeting, SEG, Expanded Abstracts, 2052–2055.

——–, 2006, Time-shift imaging condition in seismic migration: Geophysics, **71**, no. 6, S209–S217.

Sava, P., and A. Guitton, 2005, Multiple attenuation in the image space: Geophysics, **70**, no. 1, V10–V20.

Shen, P., W. Symes, S. Morton, and H. Calandra, 2005, Differential semblance velocity analysis via shot profile migration: 74th Annual International Meeting, SEG, Expanded Abstracts, 2249–2253.

Stolk, C. C., and W. W. Symes, 2004, Kinematic artifacts in prestack depth migration: Geophysics, **69**, 562–575.